Title
Investigation of Possible Wellbore Cement Failures During Hydraulic Fracturing Operations

Authors
Kim, Jihoon
Moridis, George

Publication Date
2015-05-01

Investigation of Possible Wellbore Cement Failures During Hydraulic Fracturing Operations

Jihoon Kim and George J. Moridis

Lawrence Berkeley National Laboratory
Earth Sciences Division
Berkeley CA 94720

0. Abstract

We model and assess the possibility of shear failure, using the Mohr-Coulomb model – along the vertical well by employing a rigorous coupled flow-geomechanic analysis. To this end, we vary the values of cohesion between the well casing and the surrounding cement to representing different quality levels of the cementing operation (low cohesion corresponds to low-quality cement and/or incomplete cementing). The simulation results show that there is very little fracturing when the cement is of high quality.. Conversely, incomplete cementing and/or weak cement can causes significant shear failure and the evolution of long fractures/cracks along the vertical well. Specifically, low cohesion between the well and cemented areas can cause significant shear failure along the well, but the same cohesion as the cemented zone does not cause shear failure. When the hydraulic fracturing pressure is high, low cohesion of the cement can causes fast propagation of shear failure and of the resulting fracture/crack, but a high-quality cement with no weak zones exhibits limited shear failure that is concentrated near the bottom of the vertical part of the well. Thus, high-quality cement and complete cementing along the vertical well appears to be the strongest protection against shear failure of the wellbore cement and, consequently, against contamination hazards to drinking water aquifers during hydraulic fracturing operations.

1. Introduction

Gas production from shale gas reservoirs has become an important energy resource in the future, due to the abundant amount of gas (Arthur et al. 2008; Jenkins and Boyer 2008). However, extreme low permeability of the shale gas reservoirs requires artificial reservoir stimulation to enhance productivity, such as hydraulic fracturing (Hill and Nelson 2000; Vermylen and Zoback 2011). At the same time, environmental impacts induced by the hydraulic fracturing have been raised, for example, contamination of ground water, unstable growth of the hydraulic fractures,

seismic risks and reactivation of existing faults, and soil contamination due to proppant chemicals (Zoback et al., 2010).

Dusseault et al. (2001) also studied compaction-induced shear failure of the vertical well by fluid production. Shear failure is one of the typical mechanisms of well instability. Incomplete cementing between the well and reservoir formations is considered as one of the high environmental risks of ground water contamination (Zoback et al., 2010). Pressurization at the bottom of the vertical well causes high shear stress along the vertical well and can result in shear slip at the contacting area between the well casing and the cemented zone when the contacting area is poorly cemented. Cracks from shear failure along the well can be a potential path way that can connect deep shale gas reservoirs to shallow aquifers, yielding high permeability.

Failure induced by perturbation of fluid pressure implies strong interaction between flow and geomechanics, and thus coupled flow-geomechanics simulation is required for accurate prediction and better assessment of potential risks induced by shear failure along the well. Poromechanical effect can affect perturbation of effective stress. Pressure of incompressible fluid such as water is sensitive to small change in pore volume, and, in turn, the changes in pressure alter the effective stress regime, which induces material failure (e.g, Kim et al. 2012). Permeability is also a strong function of the failure status, because material failure increases permeability significantly by several orders. For example, hydraulic fracturing increases nanodarcy of the reservoir permeability to an order of darcy, creating opening the fracture (Ji et al., 2009).

For the modeling of coupled flow and geomechanics, we use a sequential implicit method, employing the fixed-stress split, which can provide unconditional stability and high accuracy, considering two-way coupling between flow and geomechanics (Kim et al. 2011). Specifically, flow is solved first, fixing the total stress fields and considering the contribution of geomechanics to flow explicitly, and then geomechanics is solved from the solutions obtained at the previous flow step. We employ finite volume and finite element methods for flow and geomechanics in space discretization, respectively, and the backward Euler method in time discretization. We employ the Mohr-Coulomb failure model for elastoplasticity, which is widely used to model failure in cohesive frictional materials, shear failure. We then use dynamic permeability to reflect failure status every time steps. In this study, we will find that there is very little fracturing when the cementing is complete and well-done, whereas incomplete cementing can causes significant shear failure along the vertical well.

2. Mathematical description

We first describe governing equations for fluid-heat flow and geomechanics, respectively, followed by couplings in pore volume and permeability. The governing equation for multiphase and multi-component flow comes from mass balance as, (e.g., Pruess et al. (1999)),

$$\frac{d}{dt}\int_{\Omega} m^k d\Omega + \int_{\Gamma} \mathbf{f}^k \cdot \mathbf{n} d\Gamma = \int_{\Omega} q^k d\Omega \ , \tag{1}$$

where the superscript k indicates the fluid component. $d(\cdot)/dt$ means the time derivative of a physical quantity $(\cdot)$ relative to the motion of the solid skeleton. m^k is mass of component k. $\mathbf{f}^k$, and q^k are its flux and source terms on the domain Ω with the boundary Γ, respectively, where $\mathbf{n}$ is the normal vector of the boundary.

The mass of component k is written as

$$m^k = \sum_J \phi S_J \rho_J X_J^k \ , \tag{2}$$

where the subscript *J* indicates fluid phases. ϕ is the true porosity, defined as the ratio of the pore volume to the bulk volume in the deformed configuration. S_J, ρ_J, and X_J^k are saturation and density of phase *J*, and the mass fraction of component *k* in phase *J*, respectively.

The mass flux term is obtained from

$$\mathbf{f}^k = \sum_J (\mathbf{w}_J^k + \mathbf{J}_J^k) \tag{3}$$

where $\mathbf{w}_J^k$ and $\mathbf{f}_J^k$ are the convective and diffusive mass flows of component *k* in phase *J*, respectively. $\mathbf{w}_J^k$ is supplemented by Darcy's law, which includes the Klinkenberg effect for the case of gas. $\mathbf{J}_J^k$ is determined by Fick's law with diffusion and hydrodynamic dispersion.

Heat flow comes from energy (heat) balance, as

$$\frac{d}{dt}\int_\Omega m^H d\Omega + \int_\Gamma \mathbf{f}^H \cdot \mathbf{n} d\Gamma = \int_\Omega q^H d\Omega \ , \tag{4}$$

where the superscript H indicates the heat component. m^H, $\mathbf{f}^H$, and q^H are heat, its flux, and source terms, respectively. m^H in the heat accumulation term is expressed as

$$m^H = (1-\phi)\int_{T_0}^{T} \rho_R C_R dT + \sum_J \phi S_J \rho_J e_J \ , \tag{5}$$

where ρ_R, C_R, T, and T_0 are the density and heat capacity of the porous medium, temperature and reference temperature. The heat flux is written as

$$\mathbf{f}^H = -\mathbf{K}_H \mathbf{Grad} T + \sum_J h_J \mathbf{w}_J \ , \tag{6}$$

where $\mathbf{K}_H$ is the composite thermal conductivity tensor of the porous medium. **Grad** is the gradient operator. The specific internal energy, e_J, and enthalpy, h_J, in phase J become, respectively,

$$e_J = \sum_k X_J^k e_J^k \ , \ h_J = \sum_k X_J^k h_J^k \ . \tag{7}$$

Geomechanics is based on the quasi-static assumption (Coussy 1995), written as

$$\mathbf{Div}\boldsymbol{\sigma} + \rho_b \mathbf{g} = \mathbf{0}, \tag{8}$$

where **Div** is the divergence operator, $\boldsymbol{\sigma}$ is the total stress tensor, and ρ_b is the bulk density. Tensile stress is positive in this study. The infinitesimal transformation is used to allow the strain tensor, $\boldsymbol{\varepsilon}$, to be the symmetric gradient of the displacement vector, $\mathbf{u}$,

$$\boldsymbol{\varepsilon} = \frac{1}{2}\left(\mathbf{Grad}^T \mathbf{u} + \mathbf{Grad}\, \mathbf{u}\right). \tag{9}$$

Then, considering mass, energy, linear momentum balances, we focus on non-isothermal single phase flow (i.e., gas flow) with the elastoplastic geomechanics in this study, using the following constitutive relations of thermo-poro-mechanics.

3. Shear failure and coupling in permeability and porosity

Leaking of the injected water induces pressurization near the wells, as shown in Figure 1. Pressurization at the bottom of the vertical well causes high shear stress along the vertical well and can result in shear slip at the contacting area between the well casing and the cemented zone when the contacting area is poorly cemented. Shear failure along the well can create high permeable area that can connect deep shale gas reservoirs to the aquifers.

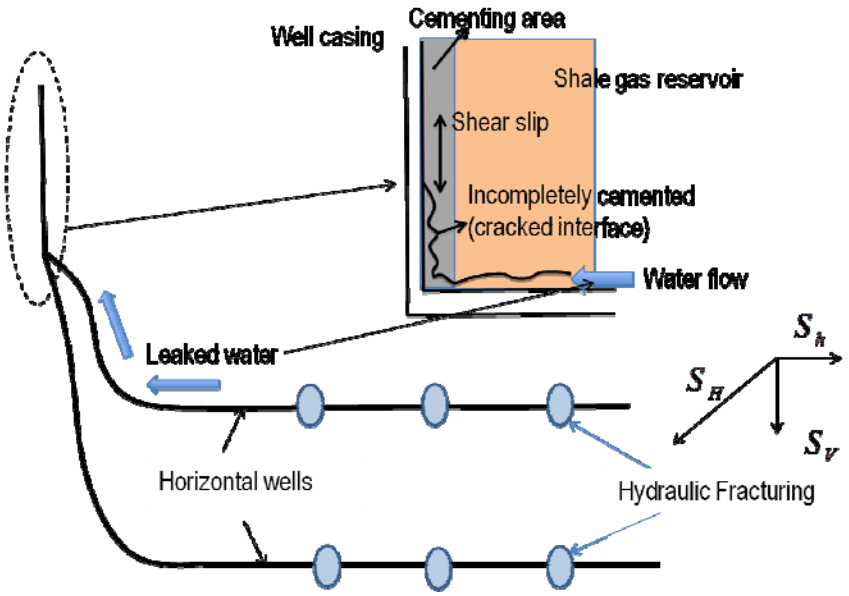

Figure. 1 Schematics of shear failure along the vertical well. S_h, S_V, S_H are the minimum horizontal, vertical, maximum horizontal total stresses, respectively The increase of pressure at the bottom can increase shear stress, which can cause shear failure and slip along the well.

For the modeling of shear failure in this study, we use the Mohr-Coulomb model, which is widely used to model failure of cohesive frictional materials. The Mohr-Coulomb model is given as

$$f = \tau'_m - \sigma'_m \sin\Psi_f - c_h \cos\Psi_f \le 0, \quad g = \tau'_m - \sigma'_m \sin\Psi_d - c_h \cos\Psi_d \le 0,$$
$$\sigma'_m = \frac{\sigma'_1 + \sigma'_3}{2}, \quad \tau'_m = \frac{\sigma'_1 - \sigma'_3}{2}, \tag{10}$$

where $\sigma_1', \sigma_2', \sigma_3'$ are the maximum, intermediate, and minimum principal effective stresses. c_h is the cohesion. f and g are the yield and plastic potential functions, respectively. Ψ_f and Ψ_d are the friction and dilation angles, respectively.

When material failure occurs, micro-fractures are created and connected, making macroscopic fractures. As a result, permeability can increase dramatically and discontinuously in time. We then consider the change in permeability, using a permeability (or transmissibility) multiplier in ω_p, as

$$\omega_p \begin{cases} = 1 & \text{if not failed} \\ >> 1 & \text{if failed} \end{cases}, \tag{11}$$

by which the intrinsic permeability, k_0 is expressed as $k_0 = \omega_p k_m$, where k_m is the intact rock permeability. Thus, the permeability is a step function for a failure status. We simply use $\omega_p = 10^4$ when the intact rock faces failure in this study.

We employ the constitutive relations for coupled multiphase non-isothermal flow and elastoplastic geomechanics, described in Coussy (1995). For elastoplastic mechanics and nonisothermal single phase flow, the constitutive relations are written as

$$\delta\boldsymbol{\sigma} = \overbrace{\mathbf{C}_e \delta\boldsymbol{\varepsilon}_e}^{\delta\boldsymbol{\sigma}'} - \alpha\delta p_f \mathbf{1} - 3\alpha_T K_{dr}\delta T\mathbf{1}, \tag{12}$$

$$\delta\zeta_f = \alpha\delta\varepsilon_v + \frac{1}{M}\delta p_f - 3\alpha_m \delta T, \tag{13}$$

$$\delta\bar{S} = \bar{s}_f \delta m_f + 3\alpha_T K_{dr}\delta\varepsilon_v - 3\alpha_m \delta p_f + \frac{C_d}{T}\delta T, \tag{14}$$

where the subscripts *e* and *f* indicate elasticity and fluid, respectively. $\boldsymbol{\sigma}'$, K_{dr}, $\mathbf{C}_e$ are the effective stress tensor, drained bulk modulus, and drained isothermal elasticity tensor, respectively. **1** is the second order identity tensor. $\delta\zeta_f = \delta m_f / \rho_f$, where ρ_f is fluid density. α and *M* are Biot's coefficient and Biot's modulus in single phase fluid, written as

$$\alpha = 1 - \frac{K_{dr}}{K_s}, \quad \frac{1}{M} = \phi c_f + \frac{\alpha - \phi}{K_s}, \tag{15}$$

where K_s is the intrinsic solid grain bulk modulus, and c_f is the fluid compressibility. $3\alpha_T$ is the volumetric thermal dilation coefficient of the solid skeleton. ε_v is the total volumetric strain. $3\alpha_m = 3\alpha_{m,\phi} + 3\alpha_{m,f}$, where $\alpha_{m,\phi}$ and $\alpha_{m,f}$ are the coefficients of thermal dilation related to porosity and fluid, respectively. $\bar{S}$ and $\bar{s}_f$ are the total entropy and the specific entropy, respectively. $C_d = C_m + m_f C_{p,f}$ is the total volumetric heat capacity, where C_m is the volumetric heat capacity of the porous medium and $C_{p,f}$ is the specific heat capacity of fluid. Symbol δ denotes variation relative to the motion of the solid skeleton.

4. Numerical Implementation

We employ the finite volume and finite element methods for flow and geomechanics in space discretization, respectively, which are widely used in reservoir and geotechnical engineerings, respectively (Aziz and Settari 1979; Lewis and Schrefler 1998). For time discretization, we use the backward Euler method, which is typically used in reservoir simulation. We use TOUGH+RealGasH2O as a fluid and heat flow simulator and ROCMECH for a geomechanics simulator, namely T+M, developed in the Lawrence Berkeley National Laboratory (Kim and Moridis, 2013), using a sequential implicit method, called the fixed-stress sequential method.

Sequential methods can offer the use of existing robust flow and geomechanics simulators only by constructing an interface between them (Settari and Mourits, 1998). According to Kim et al. (2011), the fixed stress sequential method can provide unconditional stability and high accuracy, comparable to the fully coupled methods. The fixed-stress method solves the flow problem, fixing the total stress field, where the strain and displacement fields can be changed, and considering the contribution of geomechanics to flow explicitly. Then, it solves geomechanics, based on the solutions obtained at the previous flow problem. This sequential method can easily be implemented by the Lagrange porosity function Φ and its correction $\Delta\Phi$ (e.g., Kim et al. (2012)), written as a form of the staggered approach as,

$$\Phi^{n+1} - \Phi^n = \underbrace{\left(\frac{\alpha^2}{K_{dr}} + \frac{\alpha - \Phi^n}{K_s}\right)}_{\Phi^n c_p}(p^{n+1} - p^n) + 3\alpha_T\alpha(T^{n+1} - T^n) - \underbrace{\left(\sigma_v^n - \sigma_v^{n-1}\right)}_{\Delta\Phi}, \tag{16}$$

where c_p is the pore compressibility in conventional reservoir simulation (Aziz and Settari, 1979), and σ_v is the total (volumetric) mean stress. Φ is defined as the ratio of the pore volume in the deformed configuration to the

bulk volume in the reference (initial) configuration. The porosity correction term, $\Delta\Phi$, is calculated from geomechanics, which corrects the porosity estimated from the pore compressibility. The fixed-stress sequential method solves two-way coupling between flow and geomechanics, so it captures the Mandel-Cryer effects, solving Mandel's problem correctly, which cannot be simulated by the uncoupled simulation (Kim and Moridis, 2013). When implementing the Mohr-Coulomb model, we reference the algorithms proposed by Wang et al. (2004).

5. Numerical Results

We have a full 3D domain of numerical simulation in geomechanics, as shown in Figure 2, taking a zone near the vertical well (i.e., cylindrical domain). The discretized domain has $20\times4\times50$ grid blocks in the radial, angular, and vertical direction, respectively. We use a uniform grid discretization in the z direction, where the spacing of a gridlock is 3m, while different grid spacings are used horizontally (cylindrical coordinate). Specifically, the cylindrical discretization starts with 0.06m off the origin in the racial direction, which implies that the diameter of the well casing is 0.12m. Then, the grid spacings from the well casing are 0.01m, 0.01m, 0.02m, 0.02m, 0.04m, 0.08m, 0.16m from the first to the 7th layers, and uniformly 0.3m from the 8th to 19th layers, and 1.0m for the 20th layers. In this domain of simulation, the horizontal well is assumed to be placed vertically 90m from top (z=-1440m) and changed horizontally perpendicular to the direction of the minimum compressive total stress. The area of the vertical well from -81m to -90m is assumed to be open, having high permeability. On the other hand, we take the 2D multiple interacting continuum method along the surface of the vertical well, because fluid flows along a created fracture surface of shear failure.

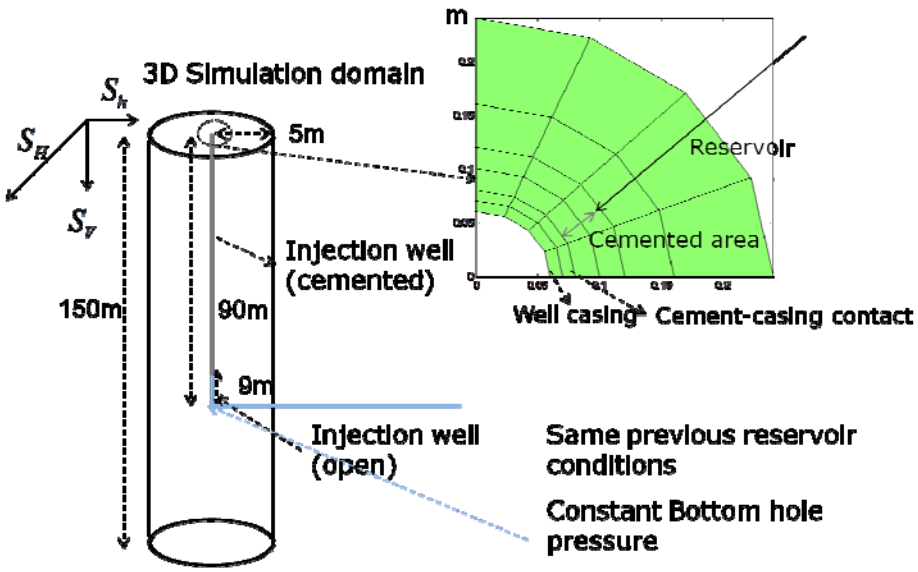

Figure 2. 3D simulation domain. We take a quarter of the cylindrical domain due to symmetry. Constant pressure due to leak from water injection is applied at -1440m of the vertical well.

For flow, we have no flow at the boundaries. The initial pressure is 17.10 MPa at 1350m in depth with the 12.44 kPa/m gradient. Initial temperature is 58.75°C at 1350 m in depth with the 0.025°C/m geothermal gradient. The heat capacities of the porous media, and the wet and dry thermal conductivities for all layers are 1000 $Jkg^{-1}{}^{o}C^{-1}$, 3.1 $Wm^{-1}{}^{o}C^{-1}$, and 0.5 $Wm^{-1}{}^{o}C^{-1}$, respectively. The initial permeability and porosity for rock (rock matrix) are $8.645\times10^{-19}m^2$, where 1 Darcy is $9.87\times10^{-13}m^2$ and 0.076, respectively.

For geomechanics, we have no horizontal displacement at the well bore side and constant traction at the outer boundary. The initial total principal stresses are -36.40MPa, and -23.30MPa, and -29.12MPa at 1350 m in depth (top of the domain) in x, y, and z directions, respectively, where the corresponding stress gradients are -27.0 kPa/m, -17.59 kPa/m, and -21.57 kPa/m, respectively. Young's modulus and Poisson' ratio of rock matrix are 12GPa and

0.3, respectively. The Biot coefficients, α, are 1.0, and the bulk densities are 2200 $kg \cdot m^{-3}$. We assume no thermal dilation in geomechanics. We use generalized reservoir models, rather than selecting geomechanical properties for a certain specific reservoir. The geomechanical properties used in this study are within a range of the properties of shale gas reservoirs (Eseme et al., 2007; Sondergeld et al., 2010). The cohesion, friction and dilation angles of rock matrix for shear failure are 10.0MPa, $\Psi_f = 28.6^0$ (0.5rad) and $\Psi_d = 28.6^0$ (0.5rad). For cementing and well (steel) casing materials, Young's moduli and Poisson's ratios are 10GPa, 200GPa, and 0.2, 0.3, respectively. For the well casing, we assume no shear failure itself, and for the cement, we take 10.0MPa, $\Psi_f = 28.6^0$ (0.5rad) and $\Psi_d = 28.6^0$ (0.5rad). We take various values of constant bottom hole pressure as well as cohesion of the contact zone between the well casing and the cement in order to test potential shear failure along the vertical well. The cohesion of the contact zone, which indicates degree of the cementing, has the same value as the cement for complete cementing, while it is lower than that of the cement for the case of incomplete cementing.

We take 30MPa of the constant bottom hole pressure with different cohesions of the contact zone; 1.0MPa, 2.0MPa, 5.0MPa, 10.0MPa. From Kim et al. (2014), the pressure at the injection point is between 30MPa and 40MPa after early time fracturing. Then, considering pressure drop between the injection point of the horizontal well and the bottom hole at the vertical well, 30MPa of the bottom hole pressure of the vertical well is assumed to be reasonable as a reference case.

We find from Figure 3 that there is little shear failure when the cohesion is high (10.0MPa). However, as the cohesion is lower, the failed zone becomes larger, propagating upward along the vertical well. In particular, fracturing is biased to the direction of the minimum total stress. From the numerical results, it is possible to make a path where reservoir fluid can easily flow up to the shallow aquifers when the cementing job is incomplete, creating cracked zones along the vertical well.

Figure 4 (left) shows the propagation of shear failure (fracture propagation). As the cohesion is lower, the failure propagation becomes faster. Although the failure propagation is fast, the injected water moves slowly along the fractured area. This indicates that gas fills the fracture area considerably. Once the fractured area is connected to the aquifer, reservoir gas can contaminate the ground water.

From Figure 5, when the bottom hole pressure is lowered to 20MPa, the fracture propagation becomes slower for the case of 1.0MPa cohesion, compared to the reference case. When we increase the bottom hole pressure, the fracture propagation becomes faster. Because the bottom hole pressure implies geomechanical loading, higher mechanical loading induces significant failure and the fast fracture propagation.

6. Conclusion

We investigated possibility of shear failure along the vertical well with rigorously coupled flow-geomechanic simulation. To this end, we varied values of cohesion between well casing and cemented areas, representing different degrees of cementing jobs. The simulation results show that there is very little fracturing when the cementing is complete and well-done, whereas incomplete cementing can causes significant shear failure along the vertical well. Even if the bottom hole pressure is increased, the complete well-cemented vertical well still show little fracturing. When the bottom hole pressure becomes lower, the fracture propagation due to weak cementing can be slower.

In conclusion, the complete cementing along the vertical well is strongly suggested in order to avoid shear failure of the well. At the same time, the lower bottom hole pressure can slow fast fracture propagation when shear failure occurs.

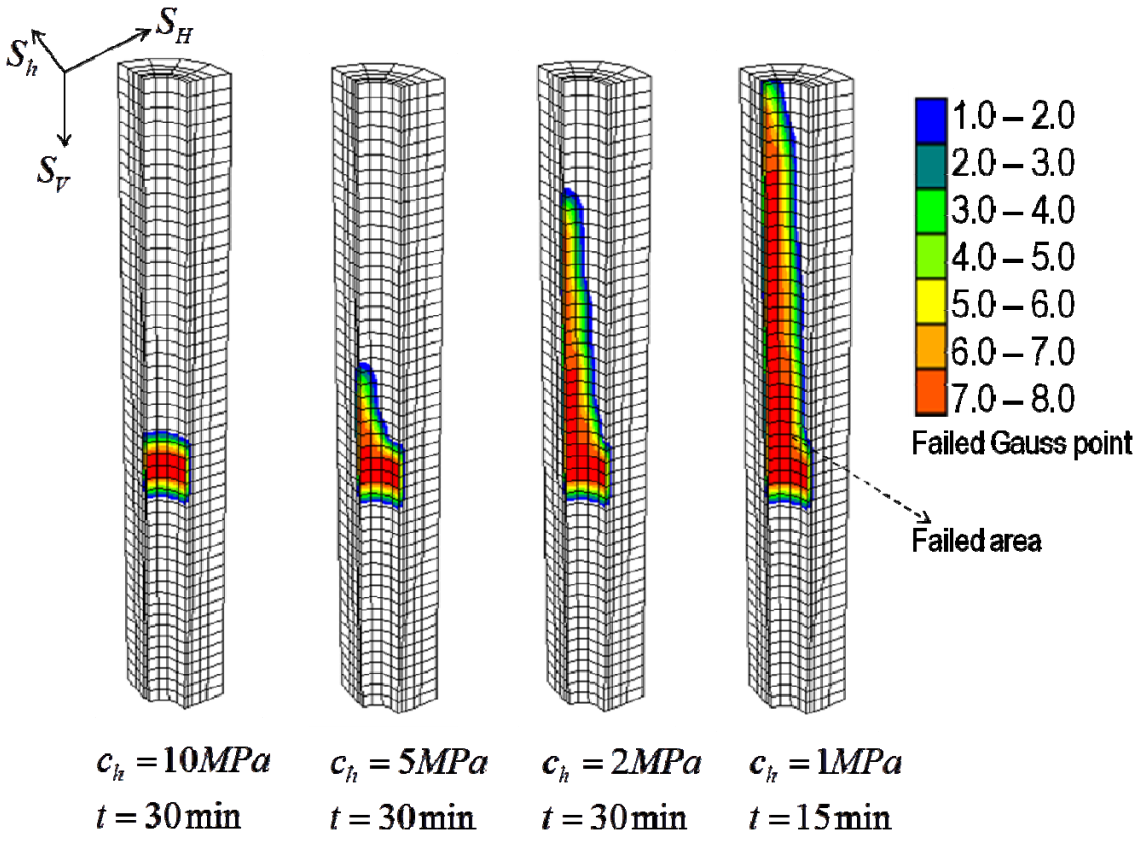

Figure 3 Failed areas due to shear failure with various cohesion values. Little failure is found for high cohesion, while low cohesion causes large failed areas.

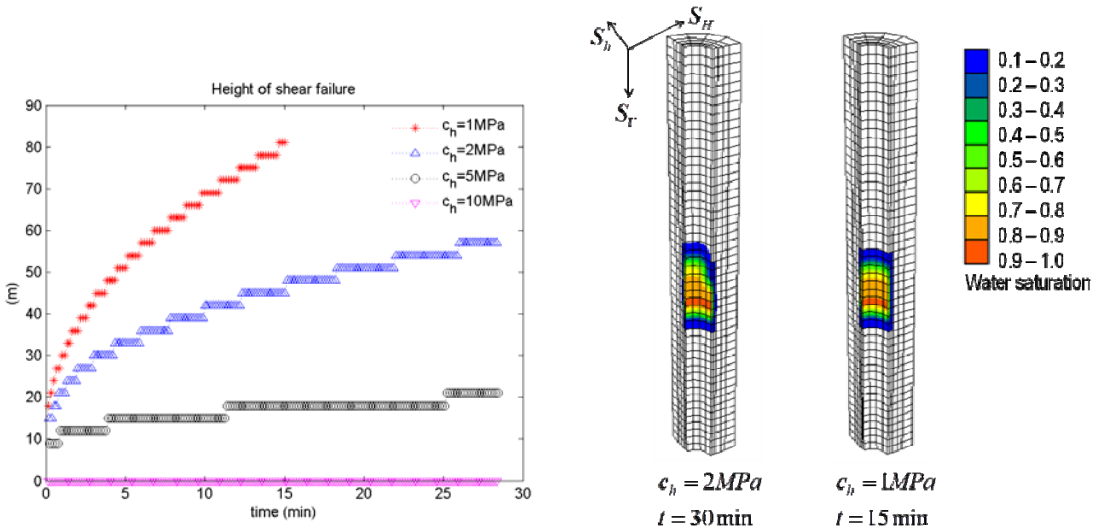

Figure 4 Left: Fracture propagation from the bottom hole along the well at the side of the minimum total stress. The lower cohesion, the faster failure propagation. Right: Water saturation area higher than the initial water saturation. Injected water only partially takes the failed area.

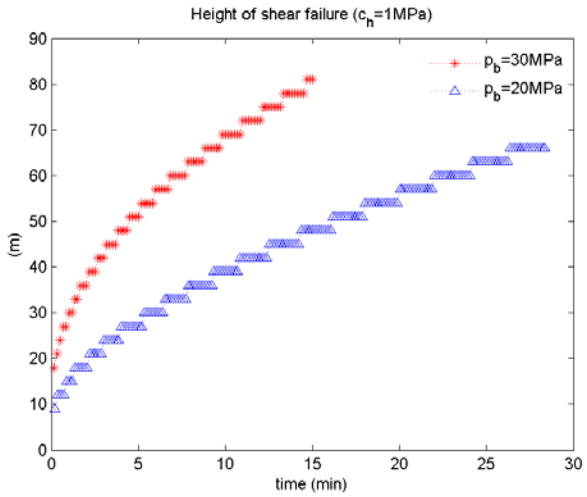

Figure 5 Fracture propagation when the bottom pressure, p_b, becomes lower. Due to relaxed mechanical loading, the fracture propagation for p_b=20MPa becomes slow.

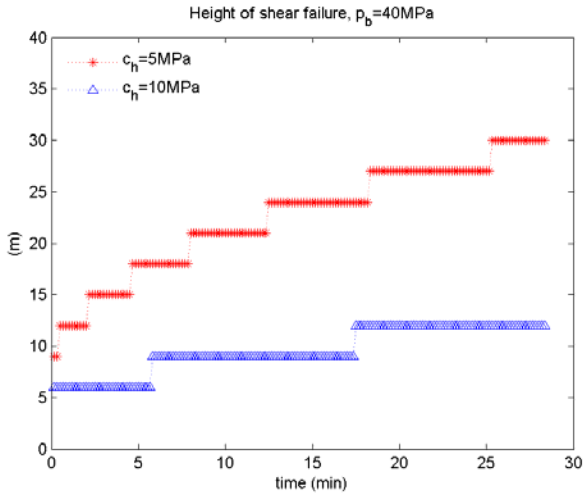

Figure 6 Fracture propagation when the bottom pressure, p_b, becomes higher, i.e., 40MPa. Due to the increased mechanical loading, the fracture propagation becomes faster than that of the reference case.

Acknowledgement

This study was supported by the US Environmental Protection Agency, Office of Water, under an Interagency Agreement with the U.S. Department of Energy at the Lawrence Berkeley National Laboratory through Contract No. DE-AC02-05CH11231, and by RPSEA (Contract No. 08122-45) through the Ultra-Deepwater and Unconventional Natural Gas and Other Petroleum Resources Research and Development Program as authorized by the US Energy Policy Act (EPAct) of 2005. The research described in this article has been funded wholly (or in part) by the U.S. Environmental Protection Agency through Interagency Agreement (DW-89-92235901-C) to the Lawrence Berkeley National Laboratory. The views expressed in this article are those of the author(s) and do not necessarily reflect the views or policies of the EPA.

References

Arthur J.D. and Bohm B. and Layne M. 2008 Hydraulic fracturing considerations for natural gas wells of the Marcellus shale. Presented at the Ground Water Protection Council 2008 Annual Forum, Cincinati, Ohio, USA, 21-24, Sep.

Aziz K. and Settari A. 1979. *Petroleum Reservoir Simulation*. London: Elsevier.

Coussy O. 1995. *Mechanics of porous continua*. Chichester, England: John Wiley and Sons.

Dusseault M.B., Bruno M.S., and Barrera J. 2001. Casing shear: Causes, cases, cures. *SPE Drilling & Completion* 16(2): 98–107. SPE-72060-PA

Eseme, E., Urai, J.L., Krooss, B. M., and Littke, R., 2007 Review of mechanical properties of oil shales: Implications for exploitation and basin modeling. *Oil Shale* **24**(2):159-174

Jenkins C.D and Boyer C.M. 2008. Coalbed- and shale-gas reservoirs. *JPT* 92-99

Hill, D.G. and Nelson, C.R.2000. Gas productive fractured shales: an overviewand update. *Gas TIPS* **6**(3), 4–13.

Ji, L., and Settari A., and Sullivan, R.B. 2009 A novel hydraulic fracturing model fully coupled with geomechanics and reservoir simulation. *SPEJ*..423-430.

Kim J. and Moridis G.J. and Yang D. and Rutqvist J.2012 Numerical studies on two-way coupled fluid flow and geomechanics in hydrate deposits. *SPEJ*.. **17**(2): 485–501. doi:10.2118/141304-PA

Kim J, and Moridis G.J. 2013 Development of the T+M coupled flow-geomechanical simulator to describe fracture propagation and coupled flow-thermal-geomechanical processes in tight/shale gas systems. *Comput. Geosci.* **60**:184-198.

Kim J., and Tchelepi H.A., and Juanes R. 2011. Stability and convergence of sequential methods for coupled flow and geomechanics: Fixed-stress and fixed-strain splits. *Comput. Methods Appl. Mech. Engrg.* 200: 1591–1606

Kim J, Um E.S., and Moridis G.J. 2014 Fracture Propagation, Fluid Flow, and Geomechanics of Water-Based Hydraulic Fracturing in Shale Gas Systems and Electromagnetic Geophysical Monitoring of Fluid Migration USA. Hydr. Frac. Tech. Conf. The woodland, TX, 4 – 6 Feb.

Lewis R.W. and Schrefler B.A. 1998. *The finite element method in the static and dynamic deformation and consolidation of porous media.* Chichester, England: Wiley, 2nd edition.

Pruess, K., C. Oldenburg, and G. Moridis, 1999 TOUGH2 User's Guide, Version 2.0, Report LBNL-43134, Lawrence Berkeley National Laboratory, Berkeley, Calif.

Settari A. and Mourits F. 1998 A coupled reservoir and geomechanical simulation system. *SPEJ*. 3:219–226.

Sondergeld C.H. and Newsham K. and Comisky J. and Rice M. and Rai C. 2010 Petrophysical considerations in evaluating and producing shale gas resources. Unconventional Gas Conf.. Pittsburgh, PA

Vermylen J.P and Zoback M.D. 2011 Hydraulic fracturing, microseismic magnitudes, and stress evolution in the Barnett Shale. USA. Hydr. Frac. Tech. Conf. The woodland, TX, 24 – 26 Jan.

Wang X. and Wang L.B. and Xu L.M. 2004 Formulation of the return mapping algorithm for elastoplastic soil models. *Comput. Geotech.* **31**:315–338.

Zoback, M., Kitasei, S., Copithorne, B.. 2010 Addressing the environmental risks from shale gas development. Worldwatch Institute Briefing Paper 1 (Worldwatch Inst,W ashington DC).